Experiments in Fluids 24 (1998) 210–224

Turbulent structure during transition to self-similarity in a round jet

T. H. Weisgraber, D. Liepmann

Abstract The developing turbulent region of a round jet was investigated using an improved implementation of digital particle image velocimetry (DPIV). The two-dimensional flow field in planes normal and parallel to the axial velocity was measured at locations between 15 and 30 diameters downstream, for two Reynolds numbers of 5500 and 16,000. The study consisted of instantaneous snapshots of the velocity and vorticity fields as well as measurements of velocity correlations up to third order. In this regime, the Reynolds number had a significant effect on both the instantaneous flow structure and the profiles of mean velocity across the jet. Coherent streamwise structures were present in the jet core for the lower Reynolds number. Additional structures whose evolution was governed by time scales two orders of magnitude larger than the convective scale inside the jet were observed in the entrainment field. The velocity correlations provided further support for the validity of DPIV turbulence measurements. The data was consistent with the equations of motion and momentum was conserved. DPIV measurements of turbulent kinetic energy components agreed with the hot-wire measurements of previous studies.

1 Introduction

The jet has played a key role in turbulent research since the early work of Liepmann and Laufer (1947). Measurements of mean velocity and higher order correlations have provided insight into the physics and served as a testbed for turbulent models. Interest has been primarily focused in the self-similar region since the theoretical problem becomes more tractable and ideally all jets will asymptotically approach this state.

Some of the most extensive experimental measurements of jet turbulence were conducted by Wygnanski and Fiedler (1969). These included profiles for mean velocities, second and third order single-point correlations, energy balances, and length scales. Later, Rodi (1975) measured mean velocity and turbulent intensity profiles using a new approach for analyzing hot-wire signals. Analysis of the results from Wygnanski and Fiedler (1969) and Rodi (1975) by Seif (1981) indicated some inconsistencies in their measurements which failed to conserve momentum as the jet evolved downstream. Capp (1983), who used laser doppler anemometry (LDA) to study jet turbulence, attributed the loss of momentum to a recirculation effect caused by the finite enclosure surrounding the jet. To verify this claim, Hussein, Capp and George (1994) recorded hot-wire and LDA measurements in a jet similar to that of Wygnanski and Fiedler but in a much larger facility. Using both stationary and moving hot-wire techniques, the investigators observed a close correspondence between the LDA and moving hot-wire measurements, while the stationary hot-wire measurements were remarkably different in the second and third order correlations. Due to the high local turbulence intensity, the stationary hot-wires were subject to cross-flow, rectification, and drop-out errors which degraded the measurements. These errors were not a factor in the LDA or moving hot-wire measurements, and the authors concluded the results from the latter techniques were more accurate. This claim was further supported by verifying the LDA and moving-hot wire data were consistent with the equations of motion and conserved momentum. In a parallel study also using moving hot-wire anemometry, Panchapakesan and Lumley (1993) also questioned the reliability of stationary hot-wires and concluded their measurements were consistent with the equations of motion. There was some discrepancies between these two most recent investigations which were attributed to different Reynolds numbers and initial conditions.

The above investigators and other turbulent modelers have been focusing on the statistical description of the self-similar region of jets for several decades. During the last 25 years, a different approach to understanding turbulence has become equally accepted, and it has become clear that coherent structures determine, to a large degree, the evolution and dynamics of turbulent flows. As a result much work, starting in 1974 with the studies of Brown and Roshko and Winant and Browand, has been focused on the developmental behavior of free shear layers and free turbulent jets. Both investigations examined the role of two-dimensional structures in the dynamics of turbulent mixing layers. Further experimental work, conducted by Roshko and co-workers (Konrad 1976, Bernal 1981, Bernal and Roshko 1986, Breidenthal 1981),

Received: *27 November 1996/Accepted*: *14 July 1997*

T. H. Weisgraber, D. Liepmann
Department of Mechanical Engineering
University of California, Berkeley
Berkeley, CA 94720, USA

Correspondence to: D. Liepmann

We would like to thank Dr. D. Fabris for providing the code and for our many discussions concerning DPIV. This work was sponsored in part by the Office of Naval Research (N0014-89-1529).

identified the three-dimensional aspects of plane shear layers generated by the evolution of streamwise vorticity. Similar results exist for jets where the behavior of the primary vortical structures were experimentally investigated by Crow and Champagne (1971) and Yule (1978). The latter research also showed the development of three-dimensional structures which were also observed by Browand and Laufer (1975). The three-dimensional structures were found to be streamwise vortices that develop in the braid region between the primary vortices similar to those in a plane shear layer (Agui and Hesselink 1988; Monkewitz et al. 1989; Liepmann 1991). Liepmann and Gharib (1992) also showed that the streamwise structures play an important role in the entrainment and growth of the jet.

A fundamental link between the coherent structures and a statistical model of turbulence is not clear. One possible approach is to investigate the transitional region of jets. This is the region between the near-field, where the flow is dominated by streamwise and Kelvin–Helmholtz-type structures, and the fully turbulent self-similar regime which contains the complete Komogorov spectrum of vortex structures. In the transitional region of a turbulent jet, the near-field vorticity has broken up into extremely complex structures and the evolution of a cascade to smaller scales has begun. In this region it may be possible to observe more clearly the interaction between the vortex dynamics and the evolution of the turbulence into similarity.

To both quantify the evolution of large-scale structures and measure the statistical properties of the developing turbulence requires a global technique that can resolve the instantaneous flow field and sufficiently sample events with the proper resolution to obtain reliable statistics. To date, hot-wire anemometry and LDA remain the most accurate methods for measuring turbulence. Their spatial and temporal resolution is unmatched by any other method, but they are limited in their scope. Attempting to map the velocity field in the transitional region without exploiting similarity would be a formidable task using single-point measurement techniques. Even if it was accomplished, the only global information would be from the statistics without any simultaneous instantaneous information. The use of single-point techniques is further complicated when attempting to measure vorticity.

Recent advances in digital particle image velocimetry (DPIV) has made this a viable alternative for turbulence measurements for moderate Reynolds number flows. Instead of the photographic method of conventional PIV, images are recorded with CCD arrays. While this results in a loss of resolution, Willert and Gharib (1991) and Westerweel (1993) have shown that this reduction in resolution does not imply a loss in accuracy. This was demonstrated by Westerweel et al. (1996) in their study of fully-developed turbulent pipe flow. They compared digital and photograpic PIV measurements with LDA data from the same facility and concluded that the accuracy of both PIV techniques was comparable. Since the flow was fully-developed, to obtain faster convergence for their statistics, Westerweel et al. (1996) sampled 100 images at a relatively slow rate of 1 Hz. They increased the number of data samples and determined the velocity statistics by averaging all the data along lines parallel to the mean flow. This was necessary because they had a limited number of images. The ability to capture and store large numbers of images makes it possible to quantify and track the motion of dominant eddies in the flow.

This paper represents a first attempt to measure, with DPIV, the development of turbulence and vorticity in the transitional region of a round jet. Two exit velocities, corresponding to Reynolds numbers of 5500 and 16,000, were used. Section 2 describes the experimental apparatus and the specifics of the DPIV method. The governing equations for this flow and the consistency checks from Hussein et al. (1994) are reviewed in Sect. 3. The instantaneous and mean fields along with the turbulent statistics are presented in Sect. 4, and are followed by the conclusions in Sect. 5.

2 Experimental method

2.1 Jet facility

The jet is modular and consists of a settling chamber and a nozzle. The nozzle is a smooth fifth-order contraction with an exit diameter of 2.54 cm, an area contraction ratio of 36 : 1, and a length-to-width ratio of 1.2. Water enters the settling chamber through a perforated pipe that injects the fluid in all directions. The large eddies are broken up by two perforated plates. Swirl or axial vorticity is then eliminated by two sets of honeycomb separated by another perforated plate. Three screens perform the final flow conditioning and filtering. Each stage is separated by approximately ten characteristic diameters from the next.

The system is a closed loop; an inline 8.9 cm impeller, powered by a 2.2 kW motor generates the flow. The flow rate is proportional to the speed of the impeller, which is controlled electronically. The nozzle velocity was calibrated using LDA. A series of four 5.1 cm pipes spaced evenly at the opposite end of the tank returns the flow to the impeller. Each pipe is perforated with small holes spread over 120°; the total area of the holes equals the cross-sectional area of the pipes. Flexible 5.1 cm tubes connect the pipes to a manifold which leads to the impeller. The jet is mounted inside a large glass-walled tank measuring $1.2 \times 1.2 \times 2.4$ m.

Near the nozzle the jet has a top-hat profile. LDA measurements indicate that the broadband turbulence intensities (RMS) at the center of the flow are approximately 0.5% including instrument noise, and a spectral analysis indicate that the flow is not forced (Liepmann and Gharib 1992). The flow characteristics and performance of the flow facility are fully described in Liepmann (1991).

2.2 Image acquisition

Figure 1 shows a diagram of the experiment and the components of the data acquisition system. To keep the flow undisturbed, all optical equipment including the camera was positioned outside the tank. Images were obtained in planes normal and parallel to the jet axis. The fluid was seeded with 80 μm fluorescein-coated polystyrene particles. A light sheet generated from a 5 W Argon ion laser illuminated the particles. The laser sheet thickness was approximately 6 mm and was shuttered to eliminate particle streaking. The images were

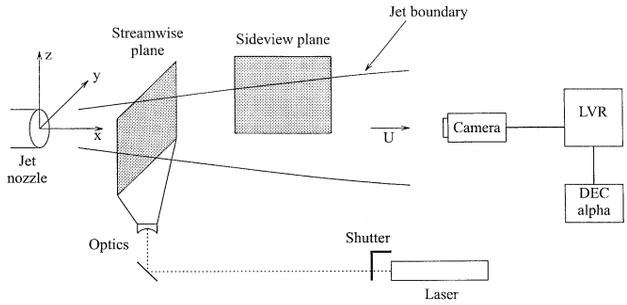

Fig. 1. Image Acquisition System

acquired at a 1134×480 pixel resolution with a Texas Instruments video camera and stored on a Sony Laser Video Recorder (LVR).

The cross-sectional images (y–z-plane) were taken with the camera facing the jet nozzle. These planes were centered on the x-axis so that the jet core and surrounding fluid were visible and extended out to a radius of approximately six diameters. The laser sheet was moved to record data at three downstream locations ($x/d = 20$, 25, and 30). At each location 2000 images were recorded at a frame rate of 30 Hz for a total time of 67 seconds.

The side-view image in the x–z-plane extended from 16 to 29 diameters in the horizontal direction. The bottom edge of the image was slightly below the jet centerline and the top edge was at approximately 6.5 diameters from the x-axis. The jet width was roughly half of the height of the side-view image plane. At this location, 1000 images were acquired for a total time of 33 s. To control the pixel displacement the camera and laser were synchronized so that the time between image pairs was 10 ms.

2.3 Image processing

During processing, each image is sub-sampled into smaller windows called interrogation zones and the velocity is measured within each zone by performing a cross-correlation with a zone in a subsequent image. The location of the cross-correlation peak with respect to the origin in correlation space determines the average particle displacement within the interrogation zone from one image to the next. Dividing by the time between images yields the mean velocity. Ideally the cross-correlation function contains a sharp peak surrounded by low level noise. Since the images are discretized, the correlation function is likewise limited to pixel resolution. Sub-pixel resolution is obtained by curve fitting nearby points to determine the location of the peak's center.

The DPIV method employed is an extension of the work of Willert and Gharib (1991). The new technique, developed by Fabris (1996), uses an iterative approach that increases the dynamic range by allowing interrogation zone shifting and reduces systematic errors by dynamically reducing zone size. The method used here also incorporates improved outlier removal which will be discussed later. The overall effect of these modifications is improved accuracy and resolution of the velocity field.

The video data from the LVR was digitized onto a 512×480 pixel grid and was transferred to a DEC Alpha computer. Both the side-view and streamwise images were processed similarly – an interrogation zone size of 32×32 pixels with a step size of 8 pixels produced a 61×57 point grid of velocity measurements. This corresponds to a spatial resolution of 4.8 mm and 5.6 mm for the side and streamwise planes, respectively. Every image was correlated only once so the effective temporal resolution of the velocity fields was reduced to 15 Hz. The processing time for a pair of images was approximately 30 s.

2.4 Post-processing

Post-processing is a necessary component of the DPIV method. When the cross-correlation is computed the ideal case of a single peak is not always realized in practice. Usually there is more than one peak and the displacement is then defined as the location of the maximum peak. In some instances, the proper peak is not selected, or none of the peaks represent what is physically happening in the flow. The resulting erroneous measurement is an outlier. The magnitude of these outliers can be equal to or as large as 100 times the magnitude of the physical flow.

Various techniques were employed to ensure the removal of these spurious measurements. When the out-of-plane motion of the particles is large compared to the thickness of the laser sheet, the zones in these regions will be poorly correlated and there is no dominant peak in the correlation function. This behaviour is seen in the jet core of the streamwise planes, especially at the higher Reynolds number. To eliminate these outliers a high-pass filter was used so that any vector with a correlation peak less than a specified threshold was set equal to zero.

Outliers can also be identified by comparing them to measurements in a small neighborhood around them. Westerweel (1993) determined that the optimal outlier detection scheme is one based upon the local median of this neighborhood. An improved method was developed by Fabris (1996), and was used for this investigation. The quality of a measurement was evaluated by comparing its magnitude and direction to the mean of a subset of the measurements contained in a 3×3 grid around it. This subset was obtained by discarding the vectors with the largest and lowest magnitudes, and the mean of the remaining vectors was defined as the local median. If the difference was greater than a certain threshold, the vector would be replaced by the local median.

In addition to spatially filtering the data with a median filter, the temporal resolution of the data was sufficient to allow a new temporal filtering method to be developed. A measurement was compared to its two closest temporal neighbors at the same grid location and substituted with an interpolated vector if the deviation exceeded a threshold value. The combination of these methods eliminated spurious vectors and provided a dataset from which reliable turbulence statistics could be calculated. While interpolation can result in a measured velocity field that is significantly smoother than the physical one, less than 5% of the data was interpolated and hence the total field remained statistically unaffected.

2.5 Turbulence calculations

DPIV measures Cartesian velocity components. To reflect the geometry of the jet, the velocities were transformed into the

radial, azimuthal, and axial components ($\tilde{v}$. $\tilde{w}$, $\tilde{u}$) of a cylindrical coordinate system centered at the jet origin. (The tilde above each component denotes the instantaneous value.) This required converting the data from the cross-sectional data sets into radial and azimuthal components. Because the jet is axisymmetric, the horizontal and vertical velocity data in the x–z-planes mapped directly to the axial and radial velocity components.

Flow statistics were computed by averaging all the velocity fields at each image plane location. Points that were removed by the correlation filter were excluded from the statistics. Profiles for the second order moments ($\overline{u^2}$, $\overline{v^2}$, $\overline{uv}$) and the third order correlations ($\overline{uuu}$, $\overline{vvv}$, $\overline{uvv}$, $\overline{vuu}$) were obtained from the side-view data (x–z-plane), while the remaining terms ($\overline{w^2}$, $\overline{vw}$, $\overline{www}$, $\overline{vww}$, $\overline{wvv}$) were calculated with the streamwise data (y–z-plane). Radial profiles for the latter quantities were obtained from a shell average along the azimuthal direction. Correlations between u and w were not determined.

At the higher Reynolds number (16,000), the out-of-plane motion in the jet core was too large to obtain a meaningful correlation between sequential images (Liepmann and Gharib 1992). As a result we were unable to calculate any statistics near the center from these images due to an insufficient ensemble size. Figure 2 shows the contours for the number of measurements remaining after correlation peak filtering as a fraction of the total number of images recorded in the y–z-plane at a distance of 20 diameters from the nozzle. At this location, the radius of the jet is approximately 2.5 diameters and the sample size is less than 50%. The effective size decreases dramatically as the centerline is approached and quickly becomes too small to be of any practical use.

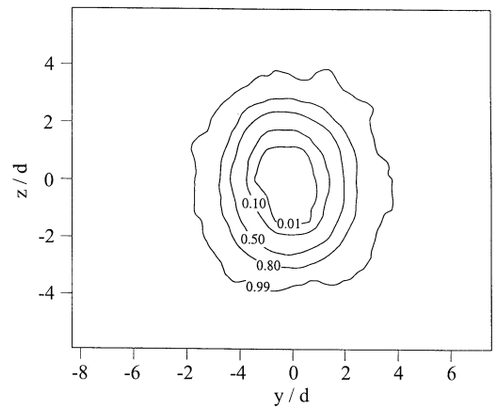

Fig. 2. Fractional number of measurements of the total ensemble. $Re = 16{,}000$, $x/d = 20$

2.6
Sources of experimental error

Determining errors of DPIV measurements is currently a very active area of research. The problem is far from trivial and depends on the properties of the seeded particles, the optical recording method, implementation of the correlation algorithm, post-processing (outlier detection and removal), and the flow under investigation. This section addresses the errors and limitations associated with the particles and spatial resolution, and the sampling error in calculating the turbulent statistics.

The 80 μm particles are neutrally buoyant with an estimated response time of 0.3 ms which is significantly smaller than the Komogorov time scales in the region under investigation for both Reynolds numbers ($\tau_k = 130$ ms for $Re = 5500$ and $\tau_k = 19$ ms for $Re = 16{,}000$). The Komogorov length scales for the lower and higher speed jet are estimated to be 0.4 mm and 0.15 mm, respectively. Since the particles are approximately half the size of the latter scale, they cannot accurately track the motion of these smaller scales. The spatial resolution of the DPIV grid determines the smallest resolved scale which is approximately 5 mm or forty times larger than the Komogorov length scale. As a result, there will be a loss of information in the large wave number region of the turbulent energy spectrum. Though this is not ideal, when considering the total range of scales in the flow, DPIV is able to resolve 93% of this range. Compared to the influence of measurement and sampling errors, it is unlikely that the energy contained in the remaining 7% of unresolved eddies is significant enough to affect the total kinetic energy or the turbulent correlations. The assumptions underlying large-eddy simulations depend on the passive role of the small scales. Hence, the absence of these scales should only adversely affect the measurement of dissipation.

Because of the finite size of the statistical ensemble, there is an error introduced when computing the mean velocity and turbulent correlations. This error depends on the number of statistically independent measurements or number of integral time scales contained in the ensemble. The integral time scale (τ_j) can be estimated from the ratio of the jet radius, δ, and the mean centerline axial velocity, U_c. The jet radius is defined where the mean velocity, U, is 25% of its centerline value. At 20 diameters downstream, this time is equal to 0.3 s for $Re = 16{,}000$ and 1 s for $Re = 5500$. For the side-views, the total acquisition time is 33 s and so there are 111 independent samples for the faster jet and 33 for the slower one. Hence the statistics for the higher Re will be more accurate.

For the streamwise views, the integral times will be slightly larger, owing to the finite thickness of the laser sheet. However, the sampling time is twice as long, 66 s, and the resulting number of independent measurements are 56 ($Re = 5500$) and 215 ($Re = 16{,}000$). This last number must be modified with the results from Fig. 2. The effective number of samples is reduced by half at the jet boundary and drops to zero near the centerline. Increasing the number of recorded images will decrease the sampling error, but this will not improve the data in the streamwise planes for the larger Reynolds number unless the shuttering time between images is significantly reduced.

3
Equations of motion and consistency of the data

The covariant and contravariant velocity components in a cylindrical coordinate system are given by $u_i = (v, rw, u)$ and $u^i = (v, w/r, u)$ respectively. For incompressible flow, the equation of mean motion in tensor notation is,

$$U^m U_{i|m} = -\frac{1}{\rho} P_{|i} - \overline{u_{i|m} u^m} + \nu g^{km} U_{i|km} \qquad (1)$$

where a vertical line indicates covariant differentation and g^{ij} are the components of the metric tensor. Capital letters refer to mean quantities and lower-case to the turbulent fluctuations.

The equations of motion can be used to validate the experimental data. Assuming the jet is axisymetric, only the radial and axial components of the momentum equations apply and they can be combined by eliminating the pressure. Upon integrating twice and ignoring terms higher than second order the following relation between the initial momentum flux per unit mass, M_0, and the momentum across the jet is obtained:

$$M_0 = 2\pi\rho \int_0^\infty [U^2 + \overline{u^2} - \tfrac{1}{2}(\overline{v^2} + \overline{w^2})]\, r\, \mathrm{d}r \tag{2}$$

The initial momentum flux is defined by $M_0 = \frac{1}{4}\pi\rho U_0^2 D^2$ where U_0 and D are the exit velocity and nozzle diameter of the jet, respectively. For a detailed derivation, see Hussein et al. (1994) or Capp (1983).

Similarly, a second order relationship for the Reynolds shear stress in terms of the mean velocity and second order correlations can also be derived:

$$\frac{\overline{uv}}{U_c^2} = \frac{1}{\eta}\frac{U}{U_c}\int_0^\eta \frac{U}{U_c}\eta'\,\mathrm{d}\eta' + \eta\left(\frac{\overline{u^2}}{U_c^2} - \frac{\overline{v^2}}{U_c^2}\right) \tag{3}$$

where $\eta = r/x$ and U_c is the mean centerline velocity. Equations (2) and (3) will be used to verify that the experimental data is consistent with the equations of motion.

The equation for turbulent kinetic energy can be obtained by subtracting the inner product of the mean velocity and Eq. (1) from the inner product of the total velocity and the Navier–Stokes equation. The result is

$$\overline{u_{i|m}u^i}U^m + \frac{1}{\rho}\overline{pu^i_{|i}} + \overline{u^i u^m u_{i|m}} - \nu g^{km}\overline{u_{i|k}u^i_{|m}} + \overline{u^i u^m}U_{i|m} + \nu g^{km}\overline{u_{i|k}u^i_{|m}} = 0 \tag{4}$$

From left to right the terms represent convection, pressure transport, turbulent transport, viscous diffusion, production, and viscous dissipation of turbulent kinetic energy. One advantage of DPIV over single-point measurement techniques is that the viscous dissipation can be determined directly without any symmetry assumption or use of Taylor's Hypothesis provided the data resolution is sufficiently high enough.

4 Results

In the statistical description of turbulence, the total instantaneous velocity is decomposed into its temporal average and a turbulent fluctuation component. Using the large, temporally-resolved velocity data sets acquired with DPIV, it is possible to investigate all three components of both the velocity and vorticity fields. Instantaneous velocity fields are of interest to demonstrate the characteristics of the raw measurements, but in general there is little information available that can be used to increase a fundamental understanding of the physics of the flow. The mean velocity and velocity correlations (e.g. Reynolds stress) provide global information that has been demonstrated in the literature from hot-wire or LDA experiments. The fluctuations are constructed as statistical measures of the local interactions due to unsteady behavior. These measurements have not been done before, especially in a global, two-dimensional sense, for a transitional jet. The vorticity is the most critical component of the dynamics of the flow especially during the transition from the near-field to the self-similar region.

4.1 Side-views

The standard way to image a jet is from the side looking normal to the primary flow direction. Figure 3 shows representative examples of the instantaneous turbulent velocity fields in the x–z-plane for Reynolds numbers of 5500 and 16,000.

The behavior of the average centerline velocity of the jet with a Reynolds number of 16,000 is shown in Fig. 4 for the range of 17 to 27 diameters. The decay is proportional to x^{-1} and the slope of 0.15 in the figure corresponds to a decay rate of 6.7. The velocity of the low-speed jet behaved similarly with a decay of 6.3. These values are slightly higher than the rates of 5.8 and 6.1, reported by Hussein et al. (1994) and Panchapakesan

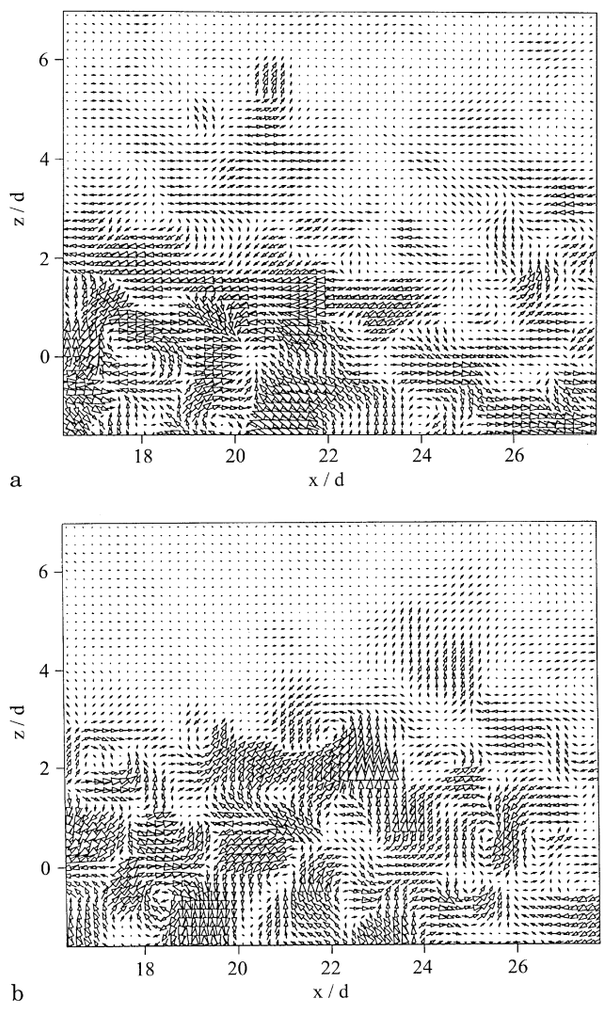

Fig. 3a, b. Turbulent velocity field in x–z plane. **a** $Re = 5500$; **b** $Re = 16{,}000$

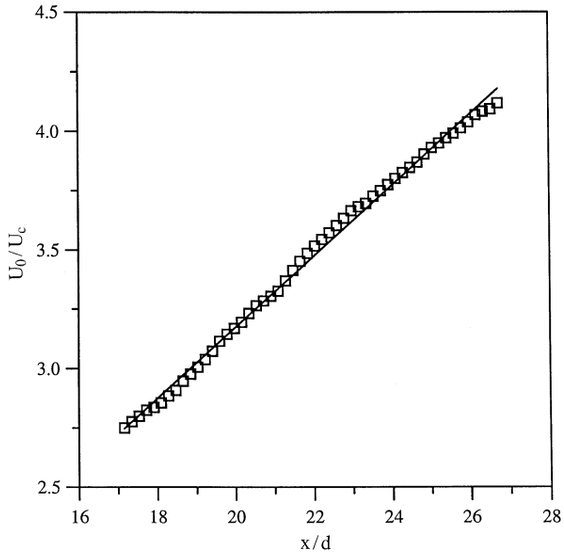

Fig. 4. Decay of the mean centerline velocity. Solid line: Least squares fit through the data ($U_0/U_c = 0.15\ x/d$). $Re = 16{,}000$

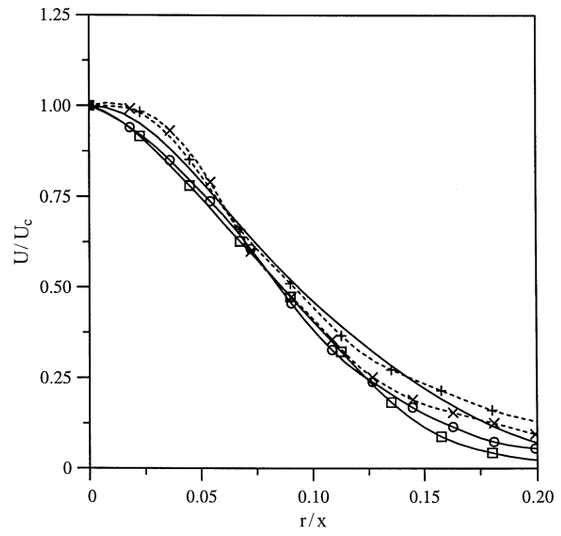

Fig. 5. Profiles of mean velocity, U, in similarity coordinates. U_c is the mean centerline velocity. Line with boxes: $Re = 16{,}000$ $x/d = 20$. Line with circles: $Re = 16{,}000$; $x/d = 25$. Dashed line with +: $Re = 5500$; $x/d = 20$. Dashed line with x: $Re = 5500$; $x/d = 25$. Solid line: Curve fit for LDA data from Hussein et al. (1994), $Re = 10^5$; $x/d = 70$

and Lumley (1993), respectively. The aforementioned results were obtained by measuring the decay rate over a range that included both the developing and self-similar regions ($x/d = 30$–120). Thus, neglecting any Reynolds number effects, it appears that during transition the centerline velocity decays faster than in the self-similar region.

The average axial velocity profile normalized by the centerline velocity, U_c, is shown in Fig. 5 for two downstream locations at both Reynolds numbers. The curve fit for the LDA data of Hussein et al. (1994) is included for comparison and is indicated by a solid line. The uncertainty in determining the mean velocity is estimated to be about 2–4% based upon the sampling error. Similarity is evident for each Reynolds number though there is some spreading at the jet boundary which is most likely due to noise. The profile for the low-speed case is not as developed as the other two and still exhibits top-hat characteristics near the centerline. Both profiles match the LDA data in center portion but slightly diverge at the jet boundary. Specifically, for the larger Reynolds number, the velocity decay at the edges is more rapid in the regions $0.08 < r/x < 0.20$ and indicates the flow is not quite fully developed. The shear layers at the edge of the jet are still more intense with a more abrupt boundary between the core and entrainment region than for a completely self-similar jet. As the jet evolves downstream and smaller scales develop, the edges become smoother in the mean.

4.2 Streamwise views

The radial and azimuthal flow behavior was investigated by viewing the jet parallel to the primary flow direction. In this view, it is also possible to investigate the dynamics of streamwise vorticity. Figure 6 shows two instantaneous velocity fields at $x/d = 20$. The data loss in the center of the jet for the high-speed case is due to effects of the correlation peak filter discussed earlier. This loss is much less significant for the low-speed jet where we are still able to resolve the motion near the center.

The average velocity fields at the same location are shown in Fig. 7. Note that the dropout zone for the higher Reynolds number is smaller in the mean, but the number of images with zones of this size is not representative of the entire sample as seen in Fig. 2. For each case a net entrainment of the surrounding fluid into the core is evident. However the presence of vortical structures in the mean of the lower speed flow is surprising. The presence of these eddies in both the jet core and the entrainment field suggests two different phenomena are occurring.

The existence of the structures in the entrainment field can be explained by again considering the integral time scales for the jet. The number of independent samples for the streamwise views given in Sect. 2.6 was based on convective scales governing the motion normal to the plane inside the jet itself. Since the entrainment motion is essentially contained in the y–z-plane, it seems appropriate to define an entrainment integral time scale as $\tau_e \sim \delta / V_m$, where V_m is the maximum mean velocity in the radial direction. For both Reynolds numbers, $V_m \sim 0.02 U_c$, and so $\tau_e \sim 50 \tau_j$. This time is 15 s for the high-speed jet and is 55 s for the lower speed. For the Reynolds number of 5500, the entrainment time scale is nearly equal to the ensemble time (66 s) and hence the streamwise eddies that evolve at the time scale τ_e appear in the mean flow. For the faster jet, no entrainment field structures were observed in the instantaneous realizations of the velocity field. Further study will be required to determine the origin of these structures and their role in the entrainment process.

From the unsymmetrical form of the mean entrainment flow in Fig. 7b it is evident that the ensemble size is too small

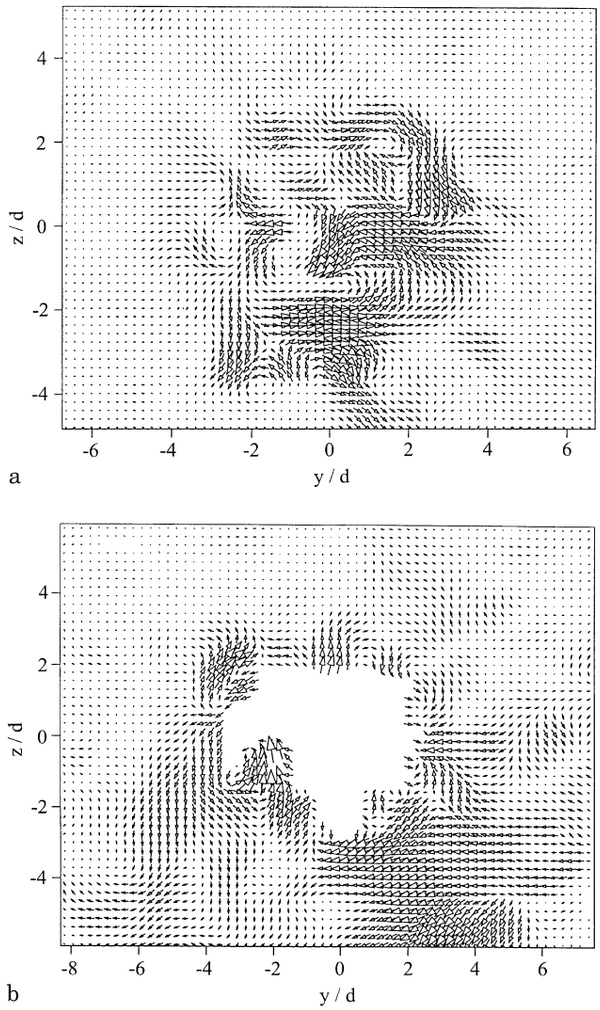

Fig. 6a, b. Turbulent velocity field in y–z plane ($x/d = 20$). **a** $Re = 5500$, **b** $Re = 16{,}000$

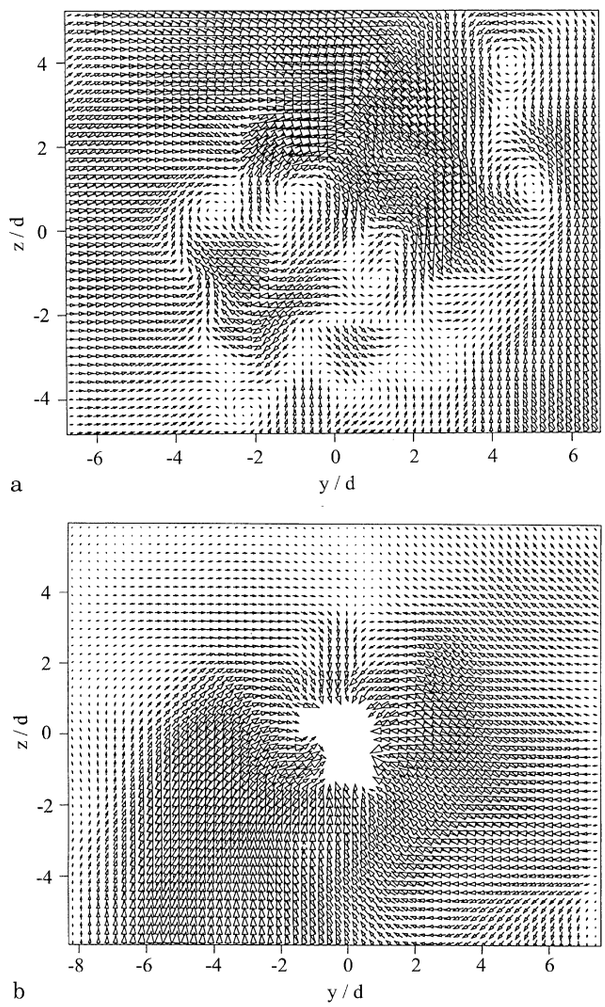

Fig. 7a, b. Mean velocity field in y–z plane ($x/d = 20$). **a** $Re = 5500$, **b** $Re = 16{,}000$

to obtain reasonable statistical convergence for the larger Reynolds number as well. Based on the entrainment integral time scale there are only four independent measurements in the ensemble. To reduce the sampling error in the entrainment field to the size of the error in the jet would require recording the flow for almost a half hour. This result has implications for the accuracy of measured entrainment rates.

The jet radius in Fig. 7a is approximately 3 diameters so the two structures in the center are located in the jet core where the motion normal to the plane is much larger than in the entrainment field. At this location, a particle moving in the x-direction at half the speed of the centerline velocity would traverse the laser sheet in a time equivalent to six consecutive frames. Any streamwise structures in the core would be convected downstream after six frames, yet these structures persist after 2000 frames. Either their axial length is very large or there is some mechanism upstream that is producing these coherent eddies inside the jet. There is no evidence of these structures further downstream, and for the higher Reynolds number, the significant out-of-plane motion in the images prevents a detailed examination of the jet core.

4.3 Vorticity

The results of the preceding section emphasize the importance of understanding the motion of coherent structures and their role in the dynamics of the jet. By calculating the vorticity fields it is possible to follow the motion of these structures. In this section we present representative mean and instantaneous vorticity fields for the velocity data presented in previous sections.

The instantaneous vorticity fields (with units s^{-1}) corresponding to Fig. 3 are shown in Fig. 8. The influence of Reynolds number on the size of the smallest flow scales is apparent in these contour plots. The vorticity associated with the smaller scales of the flow increases with Re and the eddy size decreases making the flow structures more fine. Fluctuations in the distribution of vorticity throughout the jet are apparent. For

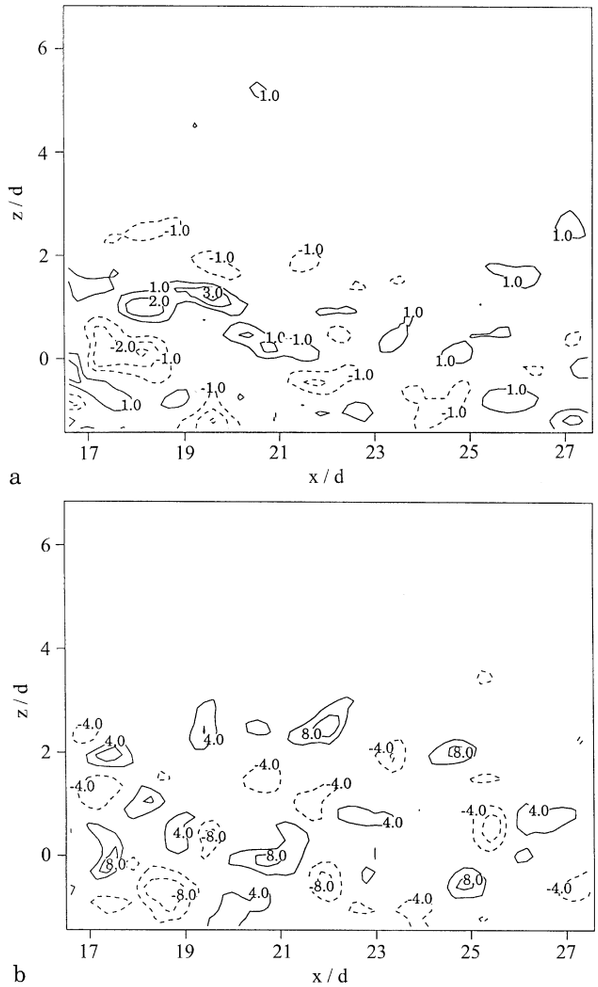

Fig. 8a, b. Instantaneous Azimuthal vorticity, ω_θ [s^{-1}]: ($x/d=20$). **a** $Re=5500$, **b** $Re=16{,}000$

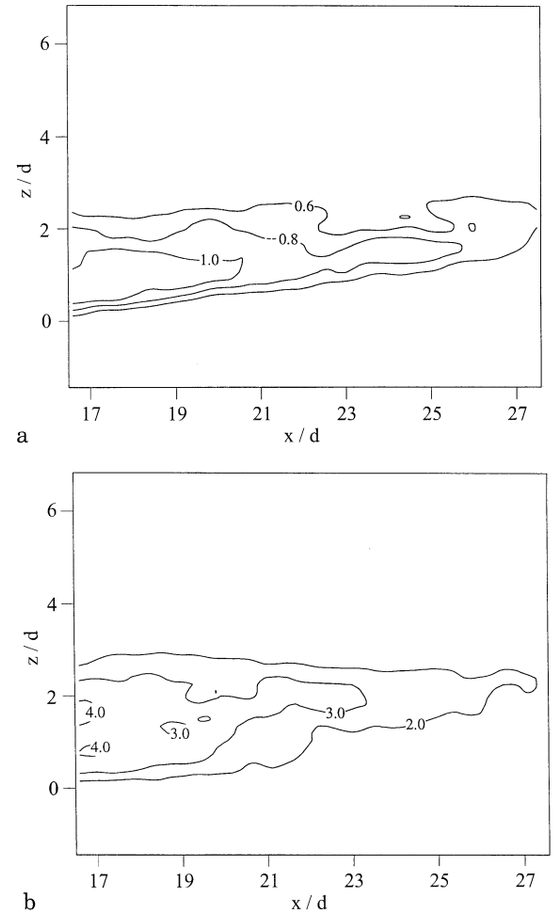

Fig. 9a, b. Mean Azimuthal vorticity field, ϖ_θ [s^{-1}]. **a** $Re=5500$, **b** $Re=16{,}000$

example, the vorticity in Fig. 8a decreases with downstream distance while the strength of the vortices are fairly consistent downstream in Fig. 8b.

Averaging the data makes the discrete eddy structures vanish, as in Fig. 9 which shows the mean azimuthal vorticity field. The vorticity is concentrated in the shear layers at the edges of the jet. This indicates that the azimuthal vorticity that developed into the primary vortical structures in the near-field of the jet still retain significant coherence after the end of the potential core as compared to the center of the flow field. The strength of the layer decreases along with the mean velocity.

Figure 10 shows contour plots of the streamwise vorticity corresponding to the velocity fields shown in Fig. 6. The magnitudes are very similar for the two speeds, which indicates the strength of the streamwise structures are less dependent on Reynolds number than the azimuthal structures. However this may be misleading since the vorticity in the inner core is not available for the higher Reynolds number. The streamwise structures are weaker than the azimuthal ones which reflects the anisotropy of the flow. The average vorticity fields are shown in Fig. 11 and are considerably weaker than the turbulent fields.

4.4 Turbulent correlations

In addition to the instantaneous fields, DPIV provides the capability to calculate the single-point correlations on the same two-dimensional grid. This section presents the turbulent statistics for the Reynolds number of 16,000 between 17 and 27 diameters downstream. The data from the slower jet was excluded because the larger effective ensemble size of the faster jet offers better statistical convergence. The correlations were determined exclusively from the side-views because of the limited information in the jet for the streamwise views (see Fig. 2). The LDA data of Hussein et al. (1994), taken at 70 diameters, is included to contrast the differences between developing and self-similar turbulence. Error bars are also included to indicate the statistical uncertainty.

There is limited data available in the literature for near-field jet turbulence. The most extensive study was conducted by

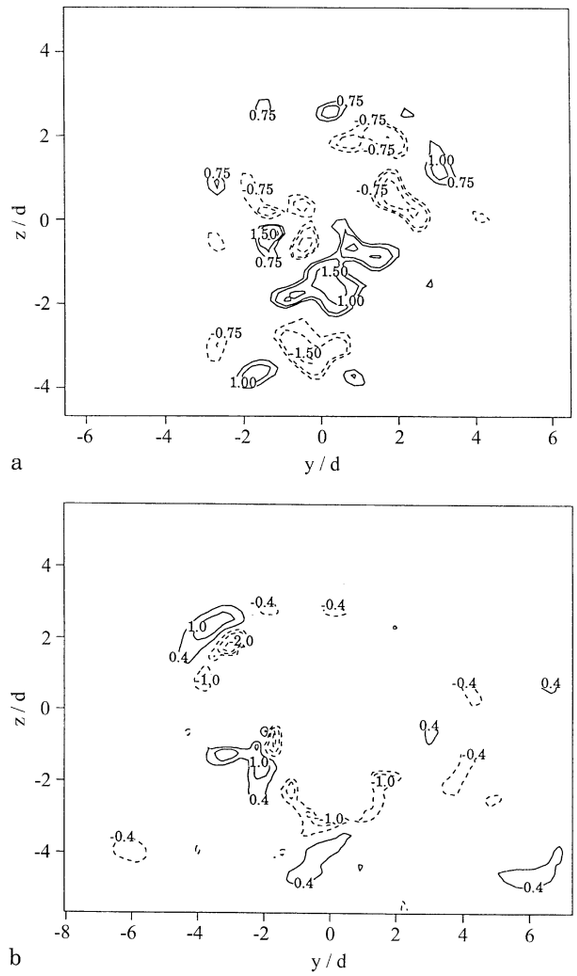

Fig. 10a, b. Instantaneous streamwise vorticity field, ω_x [s^{-1}]: ($x/d=20$). **a** $Re=5500$, **b** $Re=16{,}000$

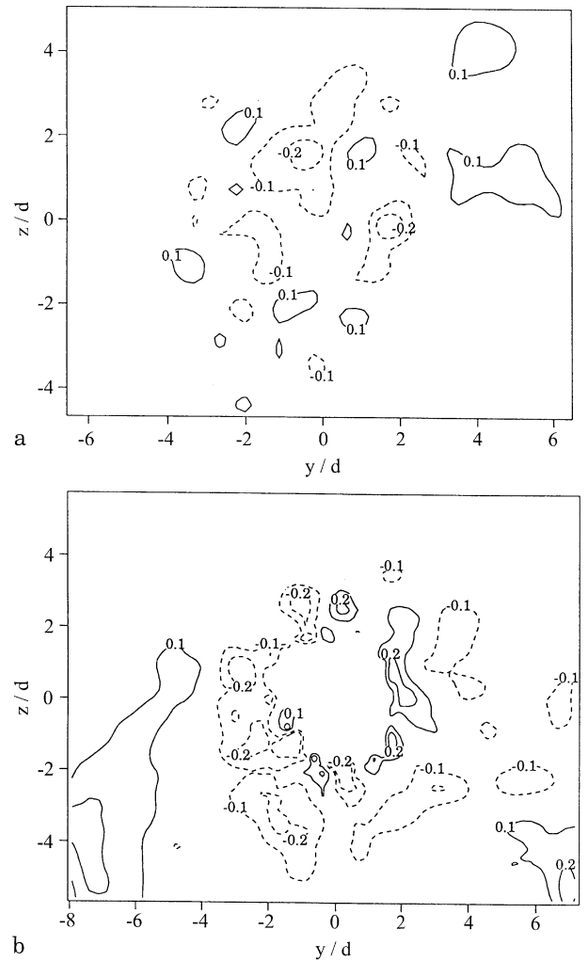

Fig. 11a, b. Mean streamwise vorticity field, ϖ_x [s^{-1}]: ($x/d=20$). **a** $Re=5500$, **b** $Re=16{,}000$

Sami, Carmody and Rouse (1967) using an air jet with a Reynolds number of 22×10^4. Their measurements included turbulent intensities, pressure fluctuations, and Taylor length scales in the region between one and twenty diameters downstream of the nozzle. However, the authors were premature in concluding the jet became self-similar after twenty diameters. The jet is still developing in this region and it is the trend toward similarity that is of primary interest in this investigation.

As an example of the two-dimensional data obtained, the contours of Reynolds stress, $\overline{uv}$, are shown in Fig. 12. The contours are normalized by the square of the mean centerline velocity and the vertical axis has been transformed into the similarity variable, r/x. Straight horizontal contours would indicate complete similarity. The increased fluctuation of the contours away from the centerline is due to measurement and statistical errors which are estimated to be approximately 3% at the centerline and 16% at $r/x=0.12$. There is also some movement of the peak value. In the remainder of this section, data is presented more conventionally, as vertical cross-sections of this surface.

The normalized axial and radial correlations along the jet centerline are shown in Fig. 13. Both quantities are increasing which indicates that self-similarity has not been attained. The axial fluctuations are approximately twice the magnitude of the radial fluctuations.

Profiles for the axial and radial correlations are shown in Figs. 14 and 15. Error bars at abscissa values of 0.08 and 0.12 indicate representative measurement and sampling errors near the centerline and jet boundary. The error varies between 3% and 12% and 4–20% for $\overline{u^2}$ and $\overline{v^2}$ respectively. As in the previous figure, the profiles do not exhibit self-similarity and increase in height with downstream location. The characteristic off-axis peak in the $\overline{u^2}$ profile is more pronounced than in the LDA data. The profile of $\overline{v^2}$ at 20 diameters downstream exhibits similar behavior while no peak is present in the self-similar measurements. The difference in magnitude between the current data and that of Hussein et al. (1994) is

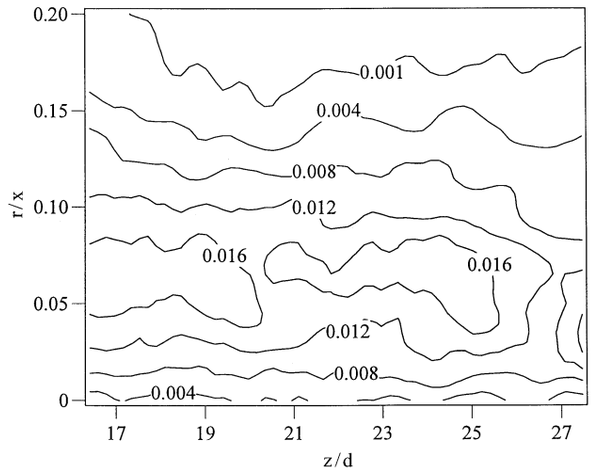

Fig. 12. Contours of constant Reynolds stress, $\overline{uv}/U_c^2$, in the x–z plane. $Re = 16{,}000$

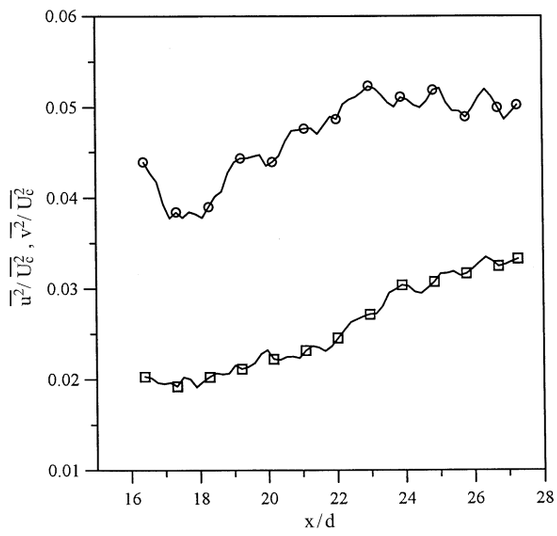

Fig. 13. Downstream development of centerline axial and radial turbulent intensities for $Re = 16{,}000$. Line with circles: $\overline{u^2}/U_c^2$. Line with squares: $\overline{v^2}/U_c^2$

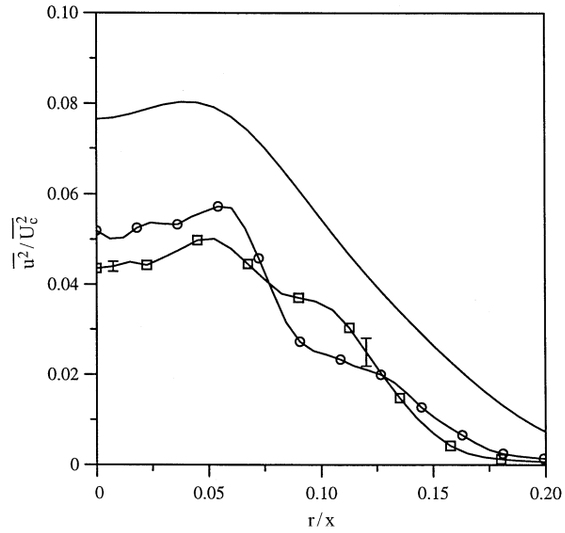

Fig. 14. Profile of $\overline{u^2}/U_c^2$ in similarity coordinates for $Re = 16{,}000$. U_c is the mean centerline velocity. Line with squares: $x/d = 20$. Line with circles: $x/d = 25$. Solid line: Curve fit for LDA data from Hussein et al., $x/d = 70$

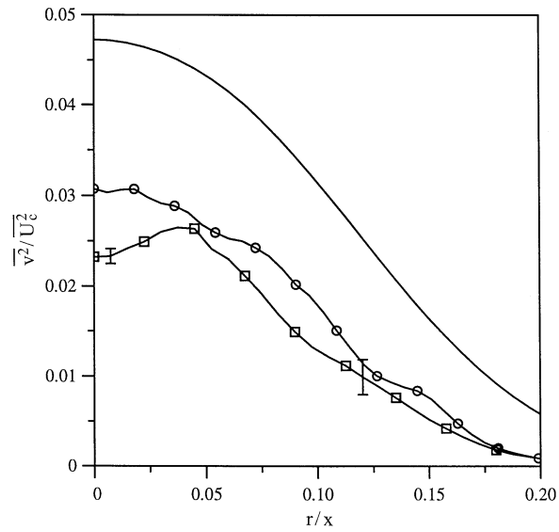

Fig. 15. Profile of $\overline{v^2}/U_c^2$ in similarity coordinates. For symbol definitions, see Fig. 14

a result of the difference in Re and because the jet is still approaching similarity in the developing region. The turbulent correlations of Hussein et al. ($Re = 10^5$) and Panchapakesan and Lumley ($Re = 1.1 \times 10^4$) differed by 5–10% in the self-similar region which could be attributed to the difference in the Reynolds number.

Comparing centerline RMS values of the axial and radial correlations with Panchapakesan and Lumley (1993) and Browne, Antonia, and Chua (1989), who tested a yaw hot-wire calibration scheme in a jet at a Reynolds number of 17,700, offers some validation for the DPIV measurements. Table 1 lists the data from all three investigations. These values compare favorably with the axial and radial intensities from DPIV.

The Reynolds shear stress, $\overline{uv}$, profile is shown in Fig. 16. In contrast to the normal stresses, the data exhibits more similarity, especially near the jet center and is closer in magnitude to the LDA data. The profile does not pass through the origin at the centerline due to some degree of uncertainty in determining the location of the jet axis in the image plane. The centerline was determined by locating the vertical position of the maximum mean velocity in the x–z-plane. The resolution

Table 1. Comparison of centerline turbulent intensities with other investigations. ($u' = \sqrt{\overline{u^2}/U_c^2}$, $v' = \sqrt{\overline{v^2}/U_c^2}$)

	Current Investigation ($x/d = 17$)	Browne et al. (1989) ($x/d = 15$)	Current Investigation ($x/d = 27$)	Panchapakesan and Lumley (1993) ($x/d = 30$)
Re	16,000	17,700	16,000	11,000
u'	0.20	0.215	0.22	0.22
v'	0.14	0.16	0.18	0.175

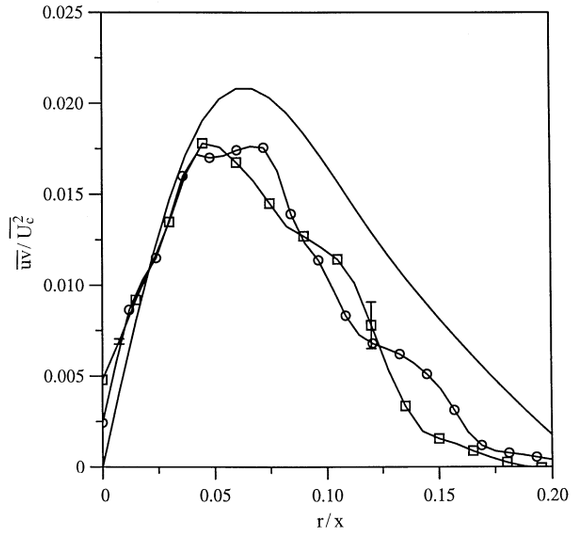

Fig. 16. Profile of Reynolds stress in similarity coordinates. For symbol definitions, see Fig. 14

of the axis is only as high as the spatial resolution of the DPIV grid (6.6 mm).

While comparison with the data of Hussein et al. (1994) is useful in contrasting the transitional and self-similar regions, it cannot provide much assessment of the validity of the DPIV measurements. The results from Table 1 are encouraging, but not quite conclusive. With the lack of relevant experimental data for comparison, the only recourse is the equations of motion. Using the second order relations given in Sect. 3, the consistency of the DPIV results with the governing equations can be evaluated.

The momentum at various locations in the jet can be compared to the initial momentum flux, M_0, at the nozzle using Eq. (2). Since data for $\overline{w^2}$ was not considered reliable it was assumed in evaluating the momentum integral that $\overline{v^2} = \overline{w^2}$. The results are listed in Table 2. The deviation from unity is between 5–12%, which is within the error range of the turbulent correlations. (The error for $\overline{uv}$ varies between 4–24%.) The deviation with the more accurate hot-wire measurements was between 3–5% (Hussein et al. 1994, Panchapakesan and Lumley 1993).

From Eq. (3), the computed value of $\overline{uv}$, based on the other second order correlations, can be compared to the DPIV measurement of the Reynolds shear stress. Both are plotted in Fig. 17 at two downstream locations. Aside from the previously mentioned error associated with axis location and the flattened peak of the data at 25 diameters, the correspondence is generally very good. With the results from Fig. 17 and Table 2, it can be concluded that the DPIV measurements are consistent with the equations of motion.

Table 2. Conservation of Momentum for $Re = 16{,}000$

x/d	M/M_0
17	0.92
21	0.88
25	0.92
27	0.95

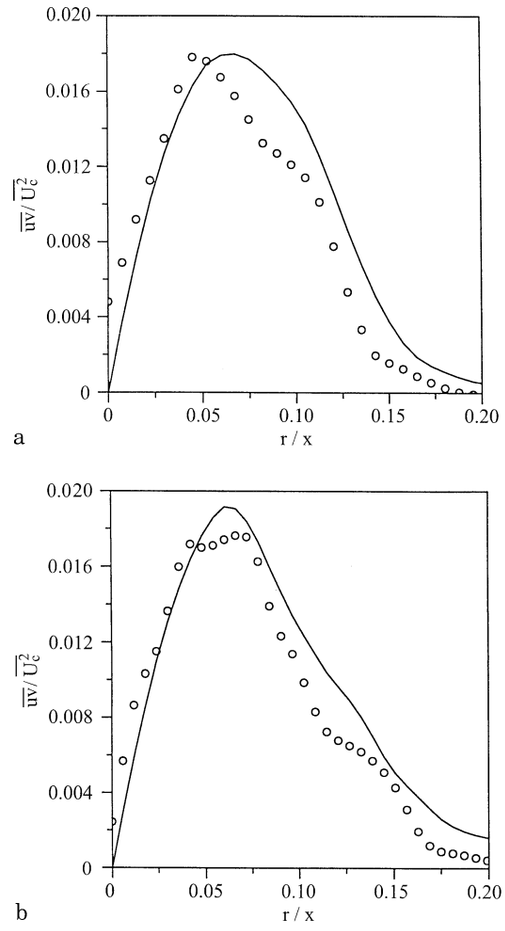

Fig. 17a, b. Comparison of Reynolds stress measured with DPIV (circles) and calculated from Eq. (3) (solid lines). **a** $x/d = 20$, **b** $x/d = 25$

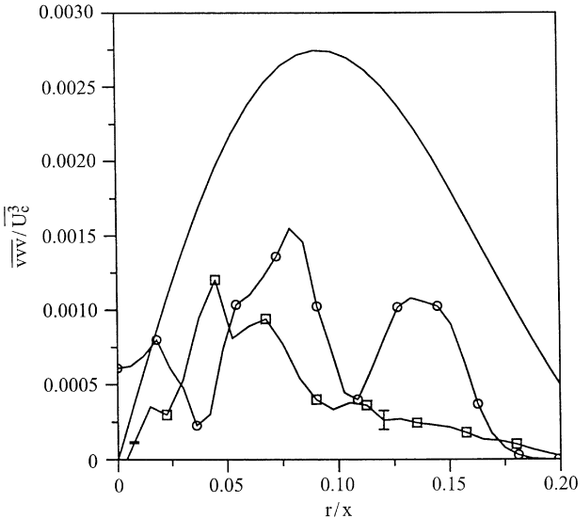

Fig. 18. Profile of $\overline{vvv}$. See Fig. 14 for symbol definitions

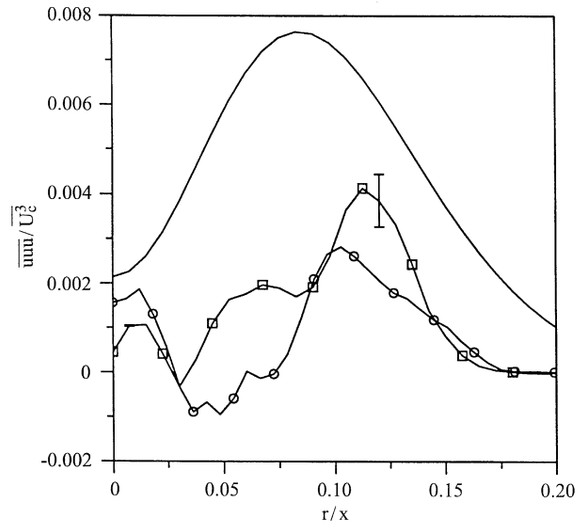

Fig. 20. Profile of $\overline{uuu}$. See Fig. 14 for symbol definitions

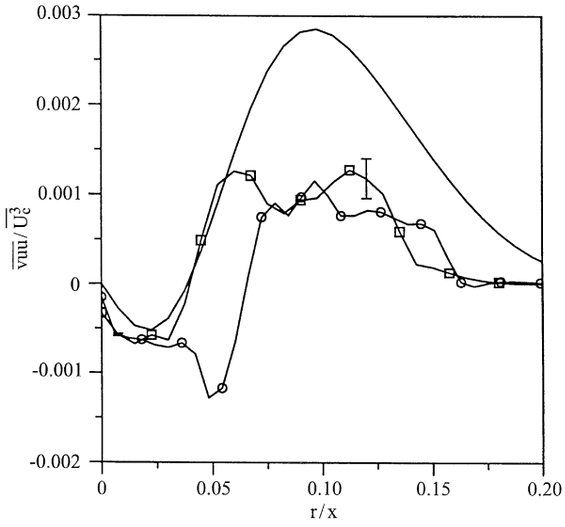

Fig. 19. Profile of $\overline{vuu}$. See Fig. 14 for symbol definitions

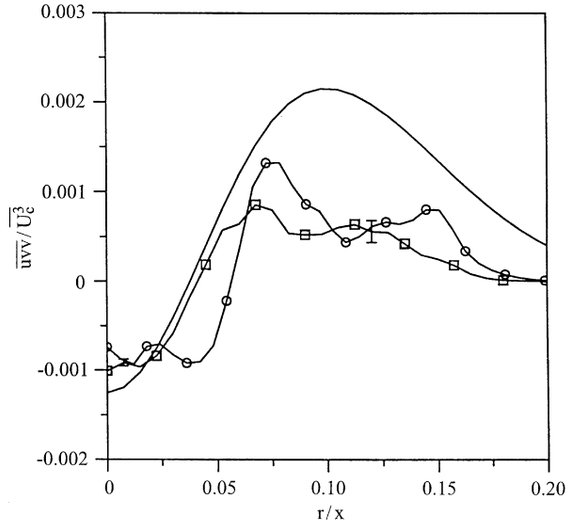

Fig. 21. Profile of $\overline{uvv}$. See Fig. 14 for symbol definitions

Figures 18–21 show the triple correlation profiles which contain more noise and exhibit much less similarity than the double correlations. The estimated error is as high as 30%. In general the peaks are significantly lower and the profiles not as broad as the LDA data. In Fig. 18, the $\overline{vvv}$ profiles are quite narrow and there is a double peak at 25 diameters. The initial dip in $\overline{vuu}$ (Fig. 19) near the centerline seen in the DPIV data is also apparent in the self-similar data, and both compare well in this region. There also is a drop near the centerline of the $\overline{uuu}$ profile in Fig. 20 which is not present in the self-similar region. The $\overline{uvv}$ profile also corresponds well with the LDA data near the centerline while at the edge it decays much more quickly which is characteristic of all the measurements in the transition region.

The stages in development of similarity in the jet is illustrated by the data in the transitional region. The mean velocity profiles exhibit the most similarity and it has been well documented that this occurs relatively early in the jet development. The second order correlations are clearly still increasing in magnitude with the Reynolds shear stress, $\overline{uv}$, being closest to its self-similar value. The third order correlations exhibit the least amount of similarity. The peak values in the transitional region are at least 50% less than the self-similar values and the shape of the profiles change downstream. While the errors

associated with the triple correlations are greater than those for the mean and second order statistics, the main cause for the difference between the DPIV and the LDA data is the lack of similarity in the developing region. These results suggest that the downstream location at which an nth-order correlation becomes self-similar is an increasing function of n.

4.5 Turbulent kinetic energy

The turbulent kinetic energy equation in its most general form is given by Eq. (4). One clear advantage to the application of DPIV to turbulence measurements is that in principle, except for the pressure correlations, all the terms in the energy budget can be directly calculated. For an axisymmetric jet all derivatives with respect to θ and the correlations $\overline{vw}$ and $\overline{uw}$ are neglected, so the energy balance simplifies to

$$\underbrace{-\frac{1}{2}\left[V\frac{\partial\overline{q^2}}{\partial r}+U\frac{\partial\overline{q^2}}{\partial x}\right]}_{\text{convection}}\underbrace{-\frac{1}{\rho}\left[\frac{1}{r}\frac{\partial}{\partial r}(r\overline{pv})+\frac{\partial}{\partial x}(\overline{pu})\right]}_{\text{pressure transport}}$$

$$\underbrace{-\frac{1}{2}\left[\frac{1}{r}\frac{\partial}{\partial r}(r\overline{vq^2})+\frac{\partial}{\partial x}(\overline{uq^2})\right]}_{\text{diffusion}}$$

$$\underbrace{-\left[\overline{v^2}\frac{\partial V}{\partial r}+\overline{w^2}\frac{V}{r}+\overline{u^2}\frac{\partial U}{\partial x}+\overline{uv}\left(\frac{\partial U}{\partial r}+\frac{\partial V}{\partial x}\right)\right]}_{\text{production}}\underbrace{-\varepsilon}_{\text{dissipation}}=0, \qquad (5)$$

where $\overline{q^2}=\overline{u^2}+\overline{v^2}+\overline{w^2}$. The dissipation is equivalent to the final term in Eq. (4). Using the data from the smaller Reynolds number flow, it was confirmed that the jet was axisymmetric and the neglected terms amounted to noise. Before differentiation the two-dimensional correlation data was fitted to a surface using a least-square method with cubic spline functions. In the side-view planes differentiation with respect to r was performed in the y direction.

The pressure correlations were not measured, and the triple correlations with $\overline{w^2}$ were neglected in the diffusion terms. Again it was assumed that $\overline{v^2}=\overline{w^2}$. Figure 22 shows the resulting energy balance at $x/d=20$ for the Reynolds number of 16,000 and is scaled by U_c^3/δ. The dissipation rate was obtained as a balance. The actual measured dissipation rate was approximately two orders of magnitude lower than the rate obtained from Eq. (5). This is due to both the size of the seeded particles and the limitation of the spatial resolution in DPIV.

The components of the energy balance in Fig. 22 correspond well with the balance at 20 diameters obtained by Sami (1967) using hot-wire measurements in a jet with a Reynolds number of 22×10^4. Quantitatively, the peak value of each component is within 15% or less of the results of Panchapakesan and Lumley (1993) in the self-similar region. The main difference is the production term which in this investigation has a higher peak value. In the energy budget of Panchapakesan and Lumley, the maximum value of the production is approximately equal to the centerline value of the convection. This difference also appears in the budget of Sami. In addition, the profile widths in the energy balance are more narrow than in the self-similar region which, as seen previously, is a characteristic difference between developing and self-similar turbulence. The favorable comparison between the energy balance obtained with DPIV and hot-wires indicates the spatial resolution of the current method is sufficient to study the dynamics and evolution of the large energy-containing eddies.

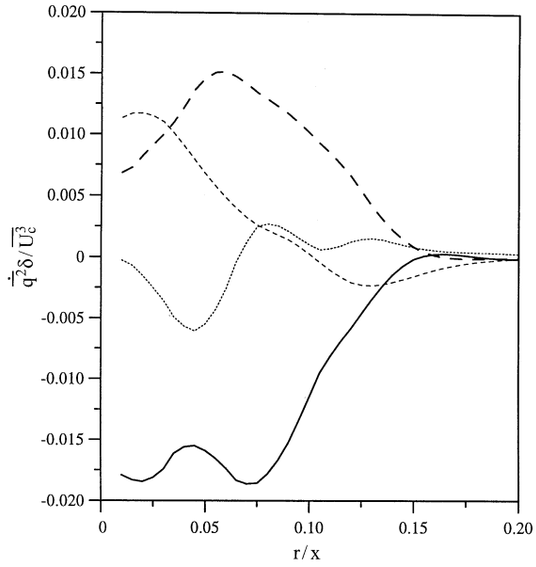

Fig. 22. Turbulent kinetic energy profile for $Re=16{,}000$ at $x/d=20$. Solid line: Dissipation. Dotted line: Diffusion. Long-dashed line: Production. Short-dashed line: Convection

4.6 Vorticity fluctuations

The normalized RMS values of the streamwise and azimuthal vorticity fluctuations are shown in Figs. 23 and 24, respectively. All profiles exhibit some similarity which is Reynolds number dependent. The decay rate in the mid-region of Fig. 24 is consistent for all the cases. The statistical errors are within 8%, but this is a conservative estimate. The overriding factor is due to the noise introduced by the limitations of the spatial resolution. The peak streamwise vorticity is slightly less than the azimuthal, however these results are undervalued since the smallest structures are not present in the measurements.

5 Conclusions

The transitional region, between 15 and 30 diameters downstream, of a round jet was examined to study the development of turbulence before reaching self-similarity. Using DPIV, the instantaneous and statistical properties of the flow were studied in the x–z and y–z planes for two Reynolds numbers.

Examination of the turbulent velocity and vorticity fields revealed the dependence of the size of the fine scale structure on Reynolds number. The Reynolds number also affected the rate of development of the jet. The shape of the mean velocity profiles for the Reynolds number of 16,000 were more characteristic of the profiles in the self-similar region while the profile of the Reynolds number of 5500 still retained a top-hat shape near the centerline. For the smaller Reynolds number,

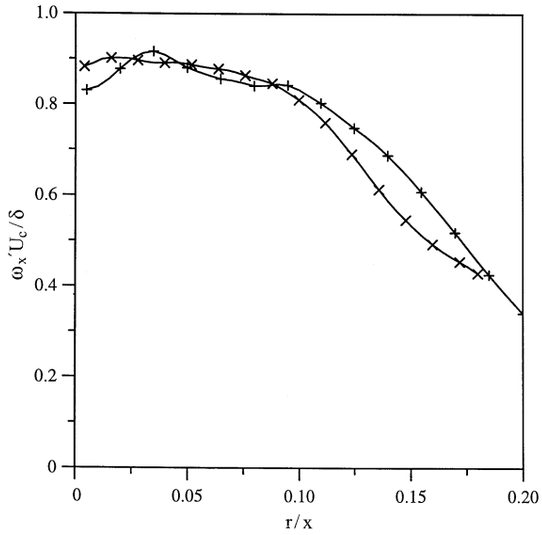

Fig. 23. Profile of turbulent streamwise vorticity intensity, $\omega_x' = \sqrt{\overline{\omega_x^2}}$. $Re = 5500$. Line with $+$: $x/d = 20$. Line with x: $x/d = 25$

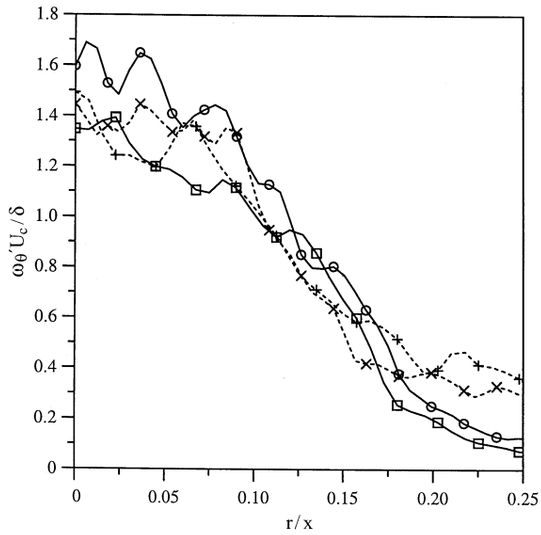

Fig. 24. Profile of turbulent azimuthal vorticity intensity, $\omega_\theta' = \sqrt{\overline{\omega_\theta^2}}$. Line with boxes: $Re = 16{,}000$ $x/d = 20$. Line with circles: $Re = 16{,}000$ $x/d = 25$. Dashed line with $+$: $Re = 5500$ $x/d = 20$. Dashed line with x: $Re = 5500$ $x/d = 25$

the mean velocity field in the y–z-plane contained eddies in both the entrainment field and jet core. These streamwise structures persisted much longer than the convective time scale and provide evidence for coherent structures in the core. A time scale was defined that describes the motion of the structures in the entrainment field which should be considered when attempting to measure entrainment rates.

The development of the flow towards similarity is a gradual process. This trend was observed by comparing the DPIV measurements with LDA data from the self-similar region. The average velocity profiles at both Reynolds numbers exhibited the most similarity. The second and third order turbulent correlations were still developing and increasing in magnitude in the downstream direction. Of the two, the second order moments, especially the Reynolds shear stress, corresponded closer to the LDA profiles. The peak production value of turbulent kinetic energy was larger than the production in the self-similar region. This behavior was also observed by Sami (1967). In the transitional region some of the turbulent kinetic energy is still localized in the shear layer as was evident by the strong off-axis peaks in the profiles of the turbulent energy components.

As a measurement technique, DPIV was effective in quantifying the turbulent properties of this flow. The data was consistent with equations of motion for the mean flow and momentum was conserved within experimental accuracy. Furthermore, there was quantitative agreement with the data of other investigations using similar Reynolds numbers. Lack of significant temporal and spatial resolution resulted in both a loss of data in the core for the higher speed jet and reduced values for the dissipation and vorticity correlations. For the Reynolds number regimes under investigations, these issues can be resolved with the advancing technology.

This implementation of DPIV has proven to be an effective tool for turbulence research. The ability to produce accurate global measurements provides the opportunity to investigate the development of local fluctuations, i.e. Reynolds stress and vorticity, and their role in the dynamics of the jet. In addition, DPIV provides the capability to study flows with more complex geometries and regions where the flow is not self-similar.

References

Agui JC; Hesselink L (1988) Flow visualization and numerical analysis of a coflowing jet: a three-dimensional approach. J Fluid Mech 191: 19–35

Bernal LP (1981) The coherent structure in turbulent mixing layers. II Secondary streamwise vortex structure. Ph.D. thesis, California Institute of Technology

Bernal LP; Roshko A (1986) Streamwise vortex structure in plane mixing layers. J Fluid Mech 170: 499–525

Breidenthal RE (1981) Structure in turbulent mixing layers and wakes using a chemical reaction. J Fluid Mech 109: 1–24

Browand FK; Laufer J (1975) The role of large scale structures in the initial development of a circular jet. In 4th Biennial Symp. on Turbulence in Liquids, Univeristy of Missouri-Rolla

Brown GL; Roshko A (1974) On density effects and large structures in turbulent mixing layers. J Fluid Mech 64: 775–816

Browne LWB; Antonia RA; Chua LP (1989) Calibration of X-probes for turbulent flow measurements. Exp Fluids 7: 201–208

Capp SP (1983) Experimental investigation of the turbulent axisymmetric jet. Ph.D. thesis, University at Buffalo, SUNY

Crow SC; Champagne FH (1971) Orderly structure in jet turbulence. J Fluid Mech 48: 547–591

Eggels JGM; Unger F; Weiss MH; Westerweel J; Adrian RJ; Friedrich R; Nieuwstadt FTM (1994) Fully developed turbulent pipe flow: a comparison between direct numerical simulation and experiment. J Fluid Mech 268: 175–209

Fabris D (1996) Combined experimental and numerical investigations of a vortex ring impinging normally on a wall. Ph.D. thesis, University of California, Berkeley

Hinze JO (1975) Turbulence. McGraw-Hill

Hussein HJ; Capp SP; George WK (1994) Velocity measurements in a high-Reynolds-number, momentum-conserving, axisymmetric, turbulent jet. J Fluid Mech 258: 31–75
Konrad JH (1976) An experimental investigation of mixing in two-dimensional turbulent shear flows with applications to diffusion-limited chemical reactions. Ph.D. thesis, California Institute of Technology
Liepmann D (1991) Streamwise vorticity and entrianment in the near field of a round jet. Phys Fluids A 3: 1179–1187
Liepmann D; Gharib M (1992) The role of streamwise vorticity in the near-field entrainment of round jets. J Fluid Mech 245: 643–668

Liepmann HW; Laufer J (1947) Investigation of free turbulent mixing. NACA Tech Note 1258
Monkewitz PA; Lehman B; Barsikow B; Bechert DW (1989) The spreading of self-excited hot jets by side-jets. Phys Fluids A 1: 446–454
Panchapakesan NR; Lumley JL (1993) Turbulence measurements in axisymmetric jets of air and helium. Part 1. Air jet. J Fluid Mech 246: 197–223
Rodi W (1975) New method of analyzing hot-wire signals in highly turbulent flow and its evaluation in round jets. Disa Info 17: 9–18
Sami S (1967) Balance of turbulence energy in the region of jet-flow establishment. J Fluid Mech 29: 81–92
Sami S; Carmody T; Rouse H (1967) Jet diffusion in the region of flow establishment. J Fluid Mech 27: 231–252
Seif AA (1981) Higher order closure model for turbulent jets. Ph.D. thesis, University at Buffalo, Suny
Tennekes H; Lumley JL (1972) A First Course in Turbulence. MIT Press, Cambridge, MA
Westerweel J (1993) Digital particle image velocimetry – theory and application. Ph.D. thesis, Technical University of Delft
Westerweel J; Draad AA; van der Hoeven JG Th; van Oord J (1996) Measurement of fully-developed turbulent pipe flow with digital particle image velocimetry. Exp Fluids 20: 165–177
Willert CE; Gharib M (1991) Digital particle image velocimetry. Exp Fluids 10: 181–193
Winant CD; Browand FK (1974) Vortex pairing: the mechanism of turbulent mixing-layer growth at moderate Reynolds number. J Fluid Mech 63: 237–255
Wygnanski I; Fiedler H (1969) Some measurements in the self-preserving jet. J Fluid Mech 38: 577–612
Yule AJ (1978) Large-scale structure in the mixing layer of a round jet. J Fluid Mech 89: 413–432